Journal of Engineering Mechanics and Machinery (2026)
Clausius Scientific Press, Canada

DOI: 10.23977/jemm.2026.110113
ISSN 2371-9133 Vol. 11 Num. 1

Research on the Calculation Method of Thermal Contact Resistance of Rough Surfaces Based on Three-Dimensional Topography Measurement and Stochastic Modeling

Gang Zhao, Jianyu Li*

School of Mechanical Engineering, Tianjin University of Science & Technology, Tianjin, 300457, China
**Corresponding Author*

Keywords: Rough Surface, Thermal Contact Resistance, Random Field Modeling Karhunen-Loeve Expansion, maximum entropy principle, Stochastic Finite Element

Abstract: The microscopic morphological characteristics of rough surfaces significantly influence Thermal Contact Resistance (TCR), exhibiting strong randomness and uncertainty at the micro-nano scale. This paper introduces a novel method for calculating thermal contact resistance that integrates three-dimensional topography data with stochastic modeling techniques. Initially, a 3D profilometer is employed to acquire the original topography data of a limited sample's rough surface, which serves as the statistical benchmark for modeling. To address the challenges of high computational complexity and the difficulty in accurately characterizing the correlation function in traditional three-dimensional random field modeling, the principle of maximum entropy, as expanded by Karhunen-Loeve(K-L), is utilized for modeling. This approach reconstructs a three-dimensional topography random field model characterized by high spatial correlation and statistical consistency. Subsequently, the Stochastic Finite Element Method (SFEM) is applied to numerically simulate the thermal contact problem based on the generated random morphology model, yielding the probability distribution and statistical evolution of the thermal contact resistance. Finally, the proposed method is validated by constructing an experimental platform for measuring thermal contact resistance. The research findings indicate that the method presented herein effectively captures the impact of random fluctuations in three-dimensional morphology on thermal contact resistance, offering an efficient and accurate approach for the quantitative evaluation and uncertainty analysis of the heat transfer performance of rough surfaces.

1. Introduction

In the domains of thermal analysis and thermal design, the issue of heat transfer at contact interfaces has consistently been a primary concern for both academic researchers and engineering practitioners. This is evident in various applications, including the thermal management of spacecraft subjected to extreme temperature differentials, the heat dissipation strategies for high-density electronic components, and the control of thermal deformation in high-precision machine tool

spindles. The efficiency of heat transfer at these contact interfaces is crucial, as it directly influences the performance stability and operational safety of the entire system. A key factor affecting this efficiency is the thermal contact resistance [1], which arises from the gaps that develop when solid surfaces fail to achieve complete adhesion. These gaps significantly hinder heat conduction, creating a "bottleneck" [2] in the heat transfer pathway.

Research on thermal contact resistance is primarily conducted through three approaches: theoretical analysis, numerical simulation, and experimental testing. The theoretical analysis emphasizes the simplification of contact morphology and thermodynamic coupling. Early investigations established various single-point contact models, including Gibson's [3] disc model and Bahrami's [4] hemispherical model. In the realm of multi-point contact modeling, Nayak [5] developed a statistical model of rough surfaces based on Gaussian stochastic processes. Numerical simulations concentrate on reconstructing rough interfaces and addressing thermal contact issues. Wang [6] examined the simulation discrepancies of Gaussian random surfaces. Zhou [7] modeled rough surfaces and explored parameter relationships. Gou [8] predicted thermal resistance by incorporating actual morphology. The objective of experimental testing is to acquire empirical data and validate the models. Cooper [9] detailed the testing methods and the thermal resistance of connection structures. Fieberg [10] employed transient infrared temperature measurements to calculate the heat transfer coefficient, Wolff [11] investigated the effects of polished surfaces and mediums.

Addressing the challenges associated with the inadequate treatment of surface morphology randomness and the lack of uncertainty quantification in traditional thermal contact resistance research, this paper presents an innovative approach. It emphasizes the importance of incorporating the randomness and uncertainty inherent in surface morphology quantification. The study specifically models the rough surface characteristics of 304 stainless steel, characterized by a surface roughness of 1.6 μm. Utilizing the principle of maximum entropy and the Karhunen-Loeve(K-L) expansion, a random field model of the rough surface was established to capture microscopic statistical features. Random finite element analysis was employed to compute the thermal contact resistance by varying the contact pressure across different random rough surface models. The proposed method underwent experimental validation through a comparison of simulation results with measured data. This research offers a comprehensive computational framework for the precise analysis of thermal contact resistance in engineering applications by integrating actual surface data, random field modeling, and uncertainty quantification.

2. Observation and data processing of rough surface topography

Rough surfaces are analyzed using amplitude parameters like R_a and R_q, as well as mixed parameters such as S_{sk} and S_{ku}. Techniques like autocorrelation function, power spectral density, and fractal dimension reveal their spatial structure. A 3D profilometer is often used for surface data collection, and a model is created through numerical reconstruction.

2.1 Surface topography treatment

The original topographical data of the rough surfaces of the limited samples were acquired using a three-dimensional profilometer. Additionally, the surface height data of the processed samples were scanned with the same profilometer. To minimize computational costs, the scanning area was set to 1mm×1mm, with a scanning interval of 0.01mm and a sampling frequency of 4500Hz. The resulting three-dimensional topographical data within the specified square area are illustrated in Figure 1.

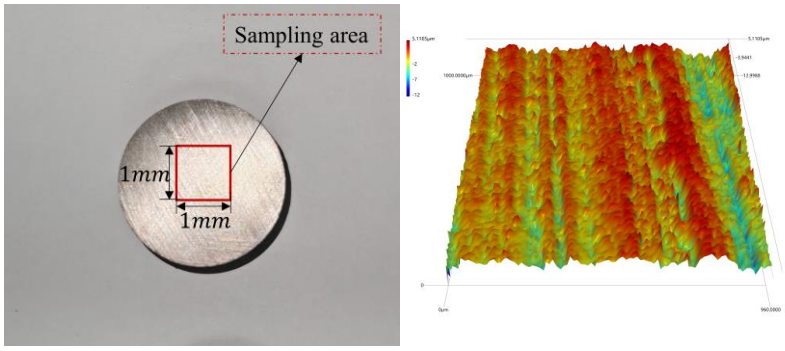

Figure 1: Sampling area and rough surface morphology.

2.2 Data extraction and processing

Determine the measurement direction along the path (1, 2, ..., m). The sampling length was selected and the sampling interval waas determined Δx. According to the sampling theorem [12], the sampling interval must be less than half of the minimum wavelength of the surface. The wavelength is derived from the Fourier transform of the surface height data, where the frequency corresponding to the peak is extracted from the spectrum, and the reciprocal is taken. [13-14]

Figure 2 illustrates the measurement schematic diagram. Equidistant points x_1, x_2,... are generated along the path. The profilometer, designated as x_t, traverses this path, recording the surface height at each point to obtain the original contour data. To ensure statistical reliability, m independent measurements (i.e., m paths) were performed on the same surface. Each path data corresponds to one row in the table.

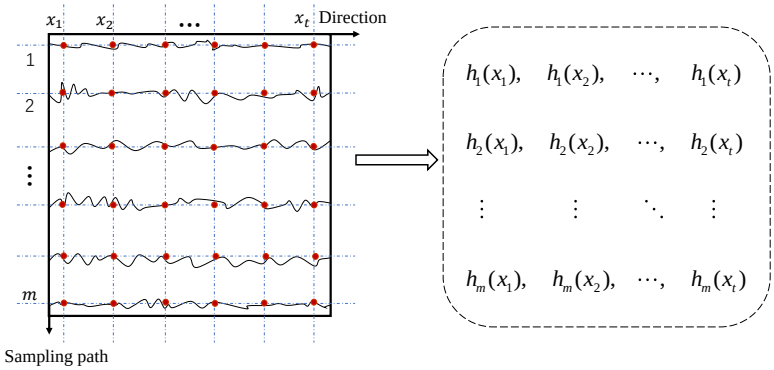

Figure 2: Measurement schematic diagram.

The roughness profile is shown in Figure 3, and the calculation of the parameter Ra.

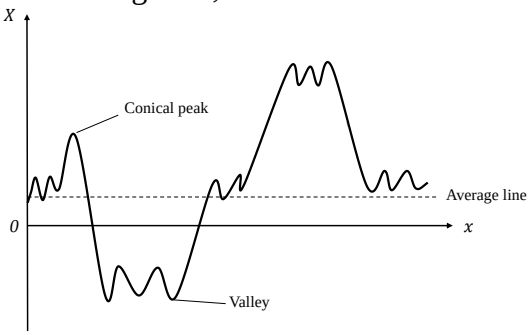

Figure 3: Schematic diagram of rough surface contour lines.

The mathematical expression for surface roughness is:

$$R_a = \frac{1}{L}\int_0^L |X - m| dx \tag{1}$$

Here, $m = \frac{1}{L}\int_0^L X dx$ represents the magnitude of the average line height. X represents the height of the surface contour line, and L represents the sampling length.

3. The stochastic modeling process of surface topography

It is assumed that the rough surface can be characterized as a random field in terms of height. The fundamental approach for reconstructing random fields from collected surface topography sample data involves several steps. First, the mean and covariance functions of the random field are derived from sample statistics [15]. Next, the K-L expansion is employed to obtain a reduced-order representation of the random field, which allows for the extraction of sample statistical information regarding the K-L random variable [16]. Given that the probability distribution of K-L random variables is unknown, the maximum entropy distribution is utilized for modeling purposes [17].

3.1 Karhunen-Loeve's rough surface random field modeling

The height distribution of a rough surface in space is represented as a random field $h(X,\omega)$, where $X=(x,y)\in R^2$ denotes the spatial coordinates, and ω signifies a random event. M independent samples were collected through measurements. The height values for each sample were recorded at N fixed measurement points, denoted as X^N, resulting in a sample matrix $H=[h_1, h_2, ..., h_M]^T$, where $h_j \in R^N$ represents the height vector of the j-th sample. K-L expansion serves as an optimal orthogonal decomposition method for characterizing random fields. Its fundamental concept involves expressing random fields as a linear combination of the mean and a collection of orthogonal random patterns. This approach depends solely on the second-order statistical characteristics of random fields and is capable of approximating the original random field using the fewest terms in the mean square sense.

First, calculate the sample mean vector $\mu \in R^N$ and the sample covariance matrix $C \in R^{N\times N}$:

$$\bar{\mu} = \frac{1}{M}\sum_{j=1}^{M} h_j \tag{2}$$

$$C = \frac{1}{M-1}\sum_{j=1}^{M}(h_j - \bar{\mu})(h_j - \bar{\mu})^{\mathrm{T}} \tag{3}$$

The covariance matrix C reflects the correlation structure of height values among different measurement points and is the basis of the K-L expansion.

Perform eigendecomposition on the covariance matrix:

$$C\phi_i = \lambda_i \phi_i, i = 1, 2, \ldots, N \tag{4}$$

Here, λ_i is the eigenvalue, and $\phi_i \in R^N$ is the corresponding orthogonal unit eigenvector, satisfying:

$$\phi_i^T \phi_j = \delta_{ij} \tag{5}$$

Then the K-L expansion of the random field at discrete points is:

$$h(\omega) = \bar{\mu} + \sum_{i=1}^{N} \sqrt{\lambda_i}\xi^{(i)}(\omega)\phi_i \tag{6}$$

In the formula, $\xi^{(i)}(\omega)$ is a random variable expanded by K-L, satisfying:

$$E[\xi^{(i)}]=0$$
$$E[\xi^{(i)}\xi^{(j)}]=\delta_{ij} \tag{7}$$

Given that the eigenvalue λ_i typically decreases rapidly with increasing i, the first q terms can be truncated and preserved to decrease the model dimension while ensuring high accuracy. The truncation order q is established based on the cumulative variance contribution rate:

Among them, the number of intercept terms $q \leqslant N$, $\sum_{i=1}^{q}\lambda_i \Big/ \sum_{i=1}^{N}\lambda_i \geq \eta$, and η is usually taken as 95% or 99%. The truncated K-L expands to:

$$h(\omega) \approx \bar{\mu} + \sum_{i=1}^{q}\sqrt{\lambda_i}\xi^{(i)}(\omega)\phi_i \tag{8}$$

For the measured M samples, the implementation of the K-L random variable corresponding to each sample h_j can be obtained by the following formula:

$$\xi_j^{(i)} = \frac{1}{\sqrt{\lambda_i}}(h_j-\bar{\mu})^{\mathrm{T}}\phi_i,\ j=1,\cdots,M,\ i=1,\cdots,q \tag{9}$$

From this, the sample matrix of the K-L random variable is obtained, where the i-th column corresponds to M observations of $\xi^{(i)}$. These samples retain the high-dimensional information of the original random field and satisfy the statistical characteristics of the equation above the equation.

3.2 The maximum entropy distribution of Karhunen-Loeve random variables

Given that the K-L variable of the measured samples may not adhere strictly to a normal distribution, we employ the maximum entropy distribution for non-parametric modeling. The random variable ξ_i is defined over the interval I, and its probability density function, denoted as $p\left(\xi^{(i)}\right)$, must satisfy the following constraints:

$$\left.\begin{aligned}\int_I p\left(\xi^{(i)}\right)d\xi = 1\\ \int_I u_i p\left(\xi^{(i)}\right)d\xi = M_i\end{aligned}\right\} \tag{10}$$

M_i is a constant, u_i is a function of the random variable ξ_i, and the density function of the maximum entropy distribution of the random variable ξ_i is:

$$f\left(x\right)=\exp\left[\lambda_0+\sum_{i=1}^{m}\lambda_i u_i\left(\xi^{(i)}\right)\right] \tag{11}$$

Combining the constraint conditions, the maximum entropy distribution of the random variable ξ_i is derived by using the Lagrange multiplier method.

3.3 Random sampling of rough surface topography

After deriving the probability density function of the K-L random variable $\xi^{(i)}(\omega)$, a new sample $\xi_{\mathrm{new}}^{(i)}$ is generated using the Markov Chain Monte Carlo (MCMC) method [18]. By substituting the

sampling results into the truncated K-L expansion, a new height field of the rough surface can be reconstructed:

$$h_{\text{new}}(\omega) = \bar{\mu} + \sum_{i=1}^{q} \sqrt{\lambda_i}\,\xi_{\text{new}}^{(i)}(\omega)\phi_i \tag{12}$$

By adjusting the sampling frequency, any number of new samples can be generated for subsequent surface performance analysis or uncertainty propagation research.

4. Thermal contact stochastic finite element analysis

As illustrated in Figure 4, the two-body contact problem is characterized by regions denoted as Ω_1 and Ω_2, which represent $\Omega = \Omega_1 + \Omega_2$. The mechanical boundary of the structure is defined as $S^{(\alpha)} = S_p^{(\alpha)} + S_u^{(\alpha)} + S_s^{(\alpha)}$, with α=1, 2 corresponding to the two contact bodies. $S_p^{(\alpha)}$ signifies the specified force boundary, $S_u^{(\alpha)}$ indicates the specified displacement boundary, and $S_c^{(\alpha)}$ represents the potential contact boundary, which is yet to be determined. For the heat transfer analysis, $\Gamma_i^{(\alpha)}(\alpha = 1,2, i = 1,2,3)$ is defined to represent the first, second, and third types of heat conduction boundary conditions, respectively. To facilitate the analysis of contact coupling effects, the contact area is designated as Ω_c. The figure also depicts the initial clearance δ^* of the contact body, where a negative value signifies an interference fit. [19-21]

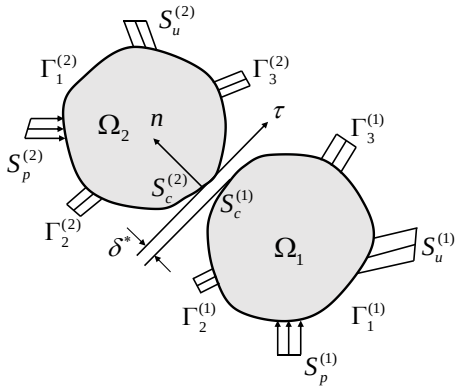

Figure 4: Two thermoelastic contact bodies.

When two solid surfaces are in contact at an interface, it is typically essential to satisfy the conditions of mechanical equilibrium and heat transfer concurrently. The unit normal vector directed from object 1 to object 2 is denoted as $\boldsymbol{n}$. The boundary conditions at the contact interface are as follows:

a) Contact conditions of force. The stress vectors on both sides of the interface are equal, that is, force equilibrium is satisfied:

$$\boldsymbol{\sigma}_1 \cdot \boldsymbol{n} = \boldsymbol{\sigma}_2 \cdot \boldsymbol{n} \tag{13}$$

Among them, $\boldsymbol{\sigma}_1$ and $\boldsymbol{\sigma}_2$ are the stress tensors of objects 1 and 2.

b) Displacement contact conditions. According to the interface contact state, displacement conditions are classified into the following situations:

Adhesive contact (no relative sliding) :

$$\boldsymbol{u}_1 = \boldsymbol{u}_2 \tag{14}$$

Sliding contact (with friction) :

$$(\boldsymbol{u}_2 - \boldsymbol{u}_1)\cdot\boldsymbol{n} = 0 \tag{15}$$

Tangential relative displacement $\boldsymbol{u}_{\mathrm{rel}}^{t}$ is related to the law of friction, such as Coulomb friction:

$$|\boldsymbol{\tau}| \leq \mu|\sigma_n| \quad When\ \ sliding \quad : \boldsymbol{\tau} = -\mu\sigma_n \frac{\boldsymbol{v}_{\mathrm{rel}}^{t}}{\left|\boldsymbol{v}_{\mathrm{rel}}^{t}\right|} \tag{16}$$

Here, $\sigma_n = \boldsymbol{n}\cdot\boldsymbol{\sigma}_1\cdot\boldsymbol{n}$, τ is the tangential stress vector, $\boldsymbol{\tau} = \boldsymbol{\sigma}_1\cdot\boldsymbol{n} - \sigma_n\boldsymbol{n}$ is the normal stress, μ is the coefficient of friction, and $\boldsymbol{v}_{\mathrm{rel}}^{t}$ is the relative tangential velocity [22].

Separation (contactless):

$$(\boldsymbol{u}_2 - \boldsymbol{u}_1)\cdot\boldsymbol{n} > 0, \sigma_n = 0 \tag{17}$$

c) Contact conditions for temperature. Non-ideal thermal contact situation:

$$T_2 - T_1 = R_{\mathrm{c}} q_{\mathrm{n}} \tag{18}$$

Here, $q_n = q_1\cdot\boldsymbol{n} = q_2\cdot\boldsymbol{n}$ represents the normal heat flux density through the interface, and Rc is usually determined by the interface roughness, pressure, gap, etc.

d)Contact conditions of heat flow. The normal heat flux density through the interface is continuous:

$$q_1\cdot\boldsymbol{n} = q_2\cdot\boldsymbol{n} \tag{19}$$

In this context, $q = -k\nabla T$ denotes the thermal conductivity. This condition must be satisfied irrespective of the presence of thermal contact resistance, indicating that there is no heat accumulation at the interface. The fundamental principle of heat conduction is rooted in the bidirectional coupling between interfacial thermal resistance and heat transfer. The efficiency of heat transfer is influenced by the microscopic contact area, resulting in a pronounced nonlinear relationship between the thermal conductivity coefficient and the macroscopic contact pressure. Heat flow can be expressed as:

$$q = k(T_1 - T_2) \tag{20}$$

Here, k denotes the thermal conductivity. In this study, a thermodynamic coupling contact model was developed using finite element software, and the numerical solution was derived through a coupled temperature-displacement analysis. The contact interface concurrently characterizes both heat conduction and mechanical contact behavior. The contact thermal conductivity is modeled as a function of contact pressure to account for the nonlinear variations in the microscopic contact area under applied load. Mechanical contact adheres to the Coulomb friction model, employing a friction coefficient of 0.2. The temperature boundary conditions are illustrated in Figure 5.

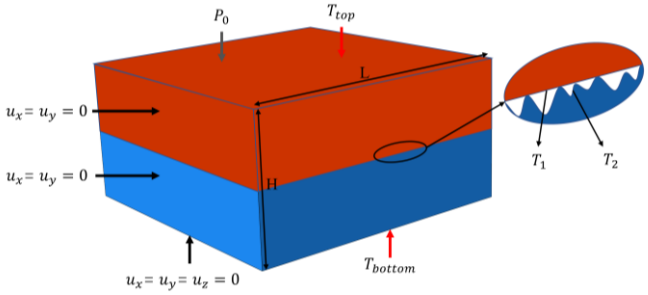

Figure 5: Boundary condition setting.

After meshing the model (Figure 6), it is essential to determine the optimal number of meshes to achieve calculation accuracy while minimizing computation time and enhancing efficiency. In this study, the grid numbers are set at 8000, 12500, 22445, 50000, and 128000, respectively. All five grid types employ identical boundary conditions.

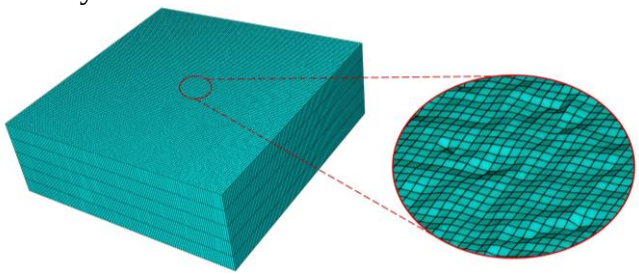

Figure 6: Grid division diagram.

When the number of grids increased from 12500 to 22445, the thermal contact resistance rose by 4.2%. However, as the grid count further increased to 50000, the thermal contact resistance exhibited only a 1.2% increase, indicating a marked decline in the growth rate. Subsequent increases in the number of grids revealed no significant changes in the calculation results, as illustrated in Figure 7. Thus, it can be concluded that a grid count of 22445 provides sufficient computational accuracy for the numerical model. Consequently, this grid scale is selected for further research.

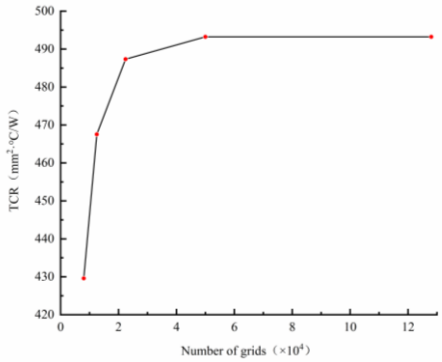

Figure 7: Diagram of thermal contact resistance varying with the number of grids.

Utilizing finite element numerical simulation alongside the principle of maximum entropy for statistical analysis, we derived the probability distribution characteristics of thermal contact resistance. This approach can also be applied to investigate the probability distribution of thermal contact resistance, as illustrated in Figure 8.

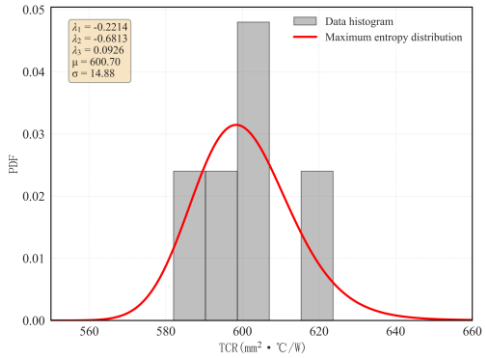

Figure 8: Thermal contact resistance distribution at 2.8MPa.

5. Case study verification

To assess the effectiveness of the method proposed in this paper for practical applications, samples were prepared for experiments and modeling. This approach aims to validate the reliability of the research process and methodology.

5.1 Sample preparation and numerical modeling

Eight cylindrical samples of 304 stainless steel were fabricated using wire cutting technology, with dimensions measuring 30 mm in diameter and 10 mm in thickness. Following surface morphology treatment, the roughness of the contact surface was maintained at approximately 1.6 μm. This stability was achieved by meticulously adjusting key process parameters, including abrasive particle size, pressure intensity, and feed rate. Through standardized material selection, precise processing, and controllable surface treatment techniques, the dimensional uniformity and stability of the surface morphology of the samples were ensured. The processed sample is illustrated in Figure 9.

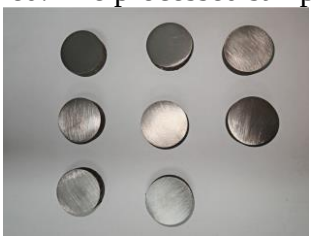

Figure 9: Processing samples.

Surface topography data for the samples were obtained using a three-dimensional profilometer, and the results of the surface roughness characterization were recorded (Figure 10). These results served as the statistical benchmark for subsequent random field modeling.

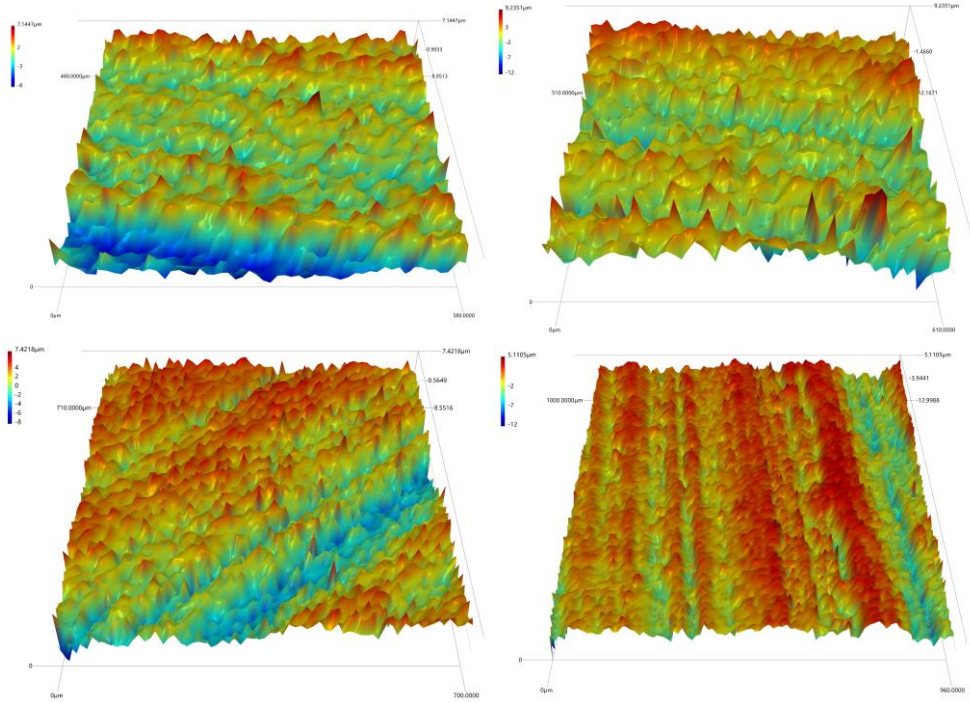

Figure 10: Surface contour of the sample.

This paper thoroughly addresses sample data selection by balancing computational efficiency and

accuracy, utilizing the first three order sample origin moments as statistical feature inputs. While ensuring computational feasibility, this approach effectively captures the overall distribution characteristics of the data. The sample integration interval is established by applying the principle of maximum entropy. Unknown parameters that align with the specified moment conditions are derived by solving the maximum entropy model. A probability density expression for the maximum entropy distribution function is formulated, incorporating moment information uniformly into the exponential function to achieve a precise approximation of the sample distribution. The reconstruction sampling results based on K-L expansion are presented in Figure 11. The distribution of the reconstructed sampling data in three-dimensional space, generated through independent sampling random coefficients, produces various implementations of the same distribution in a statistical sense, while rigorously preserving the structural integrity of the original data space.

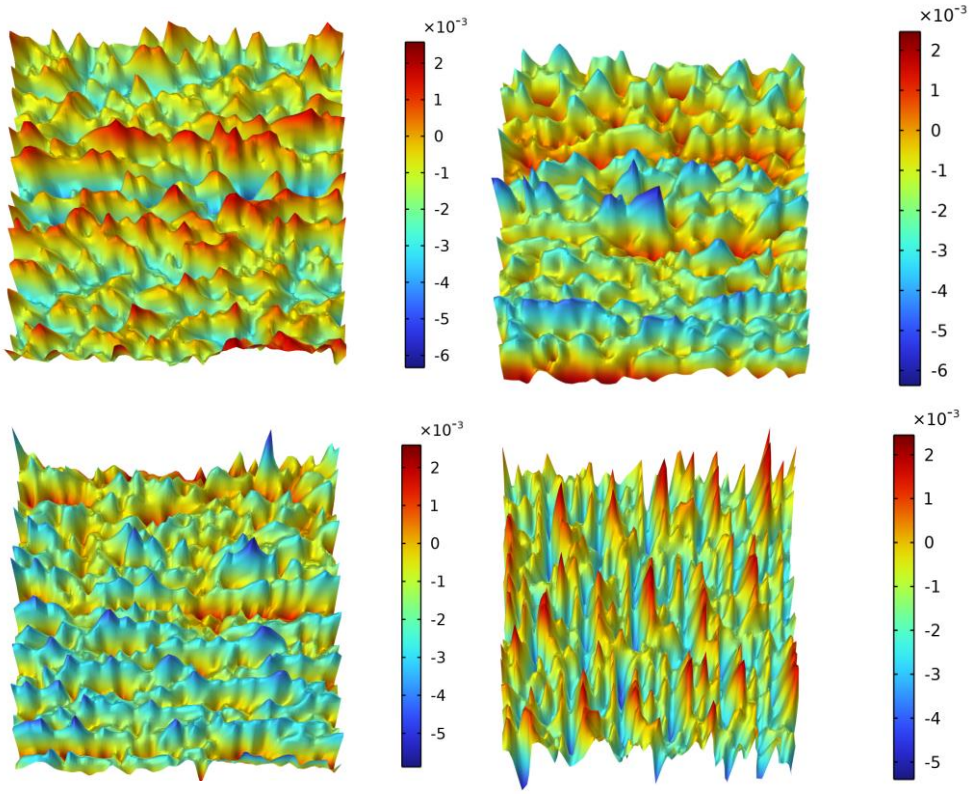

Figure 11: Reconstructed rough surfaces from sampling data.

5.2 Thermal contact resistance test

The experiment employs the steady-state method [23] to quantify the thermal contact resistance and documents the thermocouple temperature distribution as pressure varies throughout the experiment, as illustrated in Figures 12 and 13. With an increase in contact pressure, the actual contact area expands, resulting in enhanced heat transfer efficiency and a gradual reduction in the temperature difference across the interface.

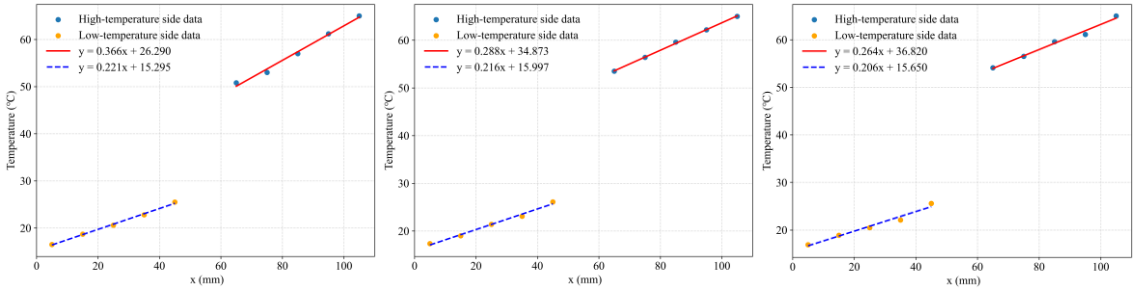

(a)2.8MPa (b)4.2MPa (c)5.5MPa

Figure 12: Temperature curve of Sample 1 heat flow meter.

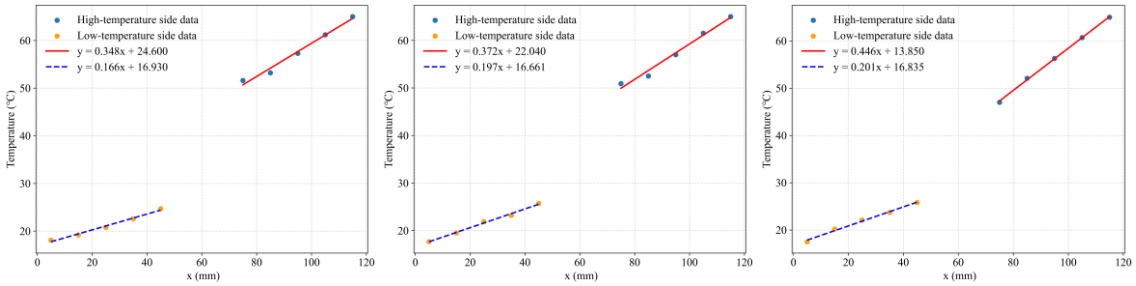

(a)2.8MPa (b)4.2MPa (c)5.5MPa

Figure 13: Temperature curves of the heat flow meters for Sample 1 and Sample 2.

In this study, we established experimental values for thermal contact resistance at pressures of 2.8 MPa, 4.2 MPa, and 5.5 MPa. The results indicate that thermal contact resistance decreases as pressure increases. This trend aligns with the physical characteristics of thermal contact resistance; specifically, increased pressure compresses the micro-protrusions on the two contact surfaces, thereby enhancing the actual contact area and effectively reducing interfacial thermal resistance.

Table 1 presents the experimental values of thermal contact resistance, illustrating the relationship between pressure and thermal contact resistance. As pressure increases, thermal contact resistance exhibits a decreasing trend.

Table 1: The experimental results of thermal contact resistance.

Pressure(MPa)	2.8	4.2	5.5
TCR($mm^2 \cdot ℃/W$)	615.934	505.308	421.253

5.3 Data verification

A finite element model of thermal contact resistance was developed. The material parameters listed in Table 2 represent the properties of the specimen. The boundary conditions are defined as follows: the upper surface experiences downward pressure, determined by the working conditions, while the lower surface is fully constrained. During the contact process under downward pressure, the upper smooth body moves exclusively in the downward direction. For the analysis of contact heat transfer, the upper boundary is maintained at 0℃, and the lower boundary is set at 47.23℃.

By defining the contact surface unit set and the node set, the heat flow and temperature are extracted from the result file. The corresponding thermal contact resistance value is then calculated using the following formula.

$$TCR = \frac{2(T_1 - T_2)}{q_1 + q_2} \tag{21}$$

In the formula presented, T_1 and T_2 denote the average temperatures of the two contacting surfaces, whereas q_1 and q_2 indicate the average heat flux densities of these surfaces.

Table 2: 304 Stainless Steel Material Physical Properties.

Density (kg/m3)	Specific heat capacity (J/(kg·K))	Thermal conductivity (W/(m·K))	Young's modulus (GPa)	Poisson's ratio	Coefficient of thermal expansion (10-6/K)	Yield stress (MPa)
7930	500	16.08	194.02	0.3	17.5	205

The thermal contact resistance of various rough surfaces exhibiting identical roughness was statistically analyzed by increasing the contact pressure, resulting in the data presented in Table 3. Surfaces with the same roughness are randomly selected, and the values of thermal contact resistance are not constant. The average value and standard deviation were subsequently calculated. The mean values in Table 4 were then compared with the experimental data, and the error rate was determined.

Table 3: The results of numerical simulation varying with pressure.

Serial number	2.8 MPa	4.2 MPa	5.5 MPa
1	598.543	487.355	401.298
2	600.562	493.063	407.372
3	582.000	472.096	399.637
4	623.669	502.062	410.827
5	598.733	487.766	400.782

Table 4: Comparison of numerical calculation results with experimental results.

Pressure(MPa)		2.8	4.2	5.5
TCR($mm^2 \cdot °C/W$)	Experiment	615.934	505.308	421.253
	Simulation	600.701	488.468	403.983
Error rate		2.47%	3.33%	4.10%

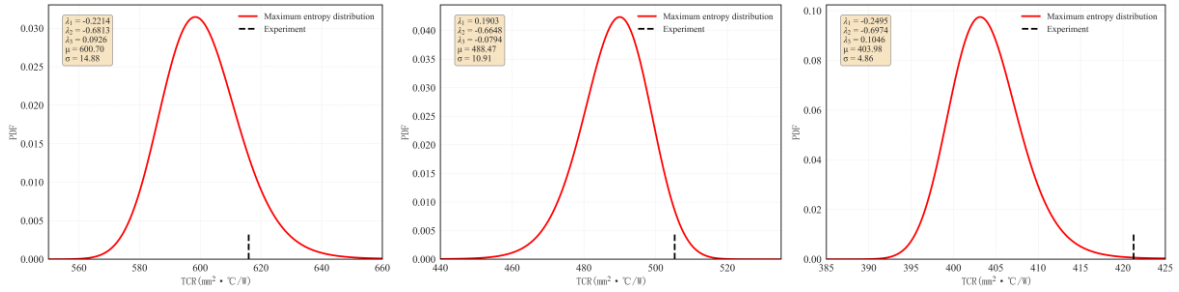

(a)2.8MPa (b)4.2MPa (c)5.5MPa

Figure 14: Thermal contact resistance distribution under three pressure conditions.

As illustrated in Figure 14, all experimental values fall within the probability distribution range derived from numerical simulations. However, the simulation results tend to be lower than the experimental values, with this discrepancy becoming more pronounced under high-pressure conditions. This deviation primarily arises from the presence of air and other impurities at the contact interface during the experiments. Under high-pressure conditions, the density of these media increases, resulting in heightened thermal resistance measurements. In contrast, the simulation model assumes a vacuum environment and does not account for the contribution of interstitial media to thermal resistance. In engineering practice, a prediction error for thermal contact resistance is

typically accepted within the range of 5% to 10%. The prediction error reported in this paper aligns with the standards required for engineering applications.

The temperature distribution and heat flux distribution results are presented in Figures 15 and 16, respectively. These figures indicate that heat transfer at the contact interfaces primarily occurs at a limited number of discrete micro-convex contact points, which represent the true contact area units.

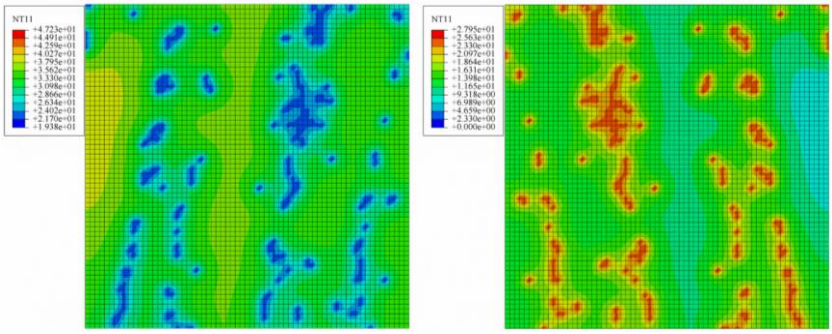

Figure 15: Temperature distribution on the contact surface.

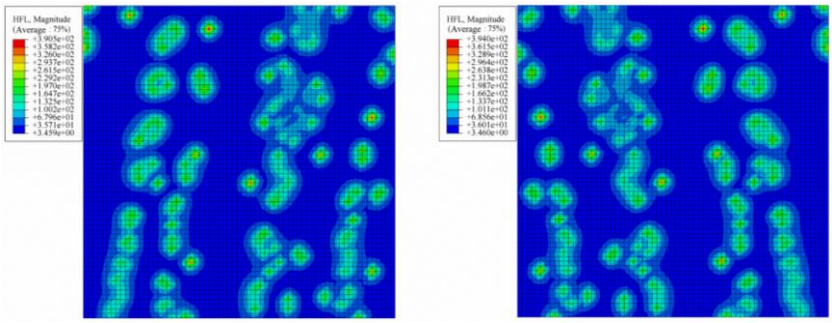

Figure 16: Heat flux distribution on the contact surface.

6. Conclusion

This paper presents a method for calculating thermal contact resistance that integrates three-dimensional topographic measurements, the K-L expansion, and the principle of maximum entropy. By developing a statistically consistent three-dimensional morphological random field model and employing stochastic finite element analysis, we conduct a quantitative and propagation analysis of the uncertainty associated with thermal contact resistance. Under pressure conditions of 2.8 MPa, 4.2 MPa, and 5.5 MPa, the relative deviations between numerical predictions and experimental values are 2.47%, 3.33%, and 4.10%, respectively, yielding an average deviation of 3.33%. The predicted values tend to be slightly lower than the experimental values, primarily due to the model's simplified treatment of material nonlinearity and the thermal resistance of the interface medium. This method effectively captures the influence of random fluctuations in surface morphology on thermal contact resistance and elucidates its probability distribution characteristics. It serves as a novel tool for the quantitative evaluation of heat transfer performance in rough interfaces. Future research will incorporate multiphysics coupling mechanisms and broaden the application scope to surfaces with varying materials and roughness levels, thereby enhancing the engineering applicability of this method.

References

[1] Greenwood J A, Williamson J B P. Contact of nominally flat surfaces[J]. Proceedings of the royal society of London. Series A. Mathematical and physical sciences, 1966, 295(1442): 300-319.

[2] Mikić B B. Thermal contact conductance; theoretical considerations[J]. International journal of heat and mass transfer, 1974, 17(2): 205-214.
[3] Gibson R D. The contact resistance for a semi-infinite cylinder in a vacuum[J]. Applied Energy, 1976, 2(1): 57-65.
[4] Bahrami M, Culham J R, Yovanovich M M, et al. Thermal contact resistance of nonconforming rough surfaces, part 2: thermal model[J]. Journal of Thermophysics and Heat Transfer, 2004, 18(2): 218-227.
[5] Nayak P R. Random process model of rough surfaces in plastic contact[J]. Wear, 1973, 26(3): 305-333.
[6] Wang Y, Azam A, Wilson M C T, et al. A comparative study for selecting and using simulation methods of Gaussian random surfaces[J]. Tribology International, 2022, 166: 107347.
[7] Zhou W, Tang J, He Y, et al. Modeling of rough surfaces with given roughness parameters[J]. Journal of Central South University, 2017, 24(1): 127-136.
[8] Gou J J, Ren X J, Dai Y J, et al. Study of thermal contact resistance of rough surfaces based on the practical topography[J]. Computers & Fluids, 2018, 164: 2-11.
[9] Cooper M G, Mikic B B, Yovanovich M M. Thermal contact conductance[J]. International Journal of heat and mass transfer, 1969, 12(3): 279-300.
[10] Fieberg C, Kneer R. Determination of thermal contact resistance from transient temperature measurements[J]. International Journal of Heat and Mass Transfer, 2008, 51(5-6): 1017-1023.
[11] Wolff E G, Schneider D A. Prediction of thermal contact resistance between polished surfaces[J]. International Journal of Heat and Mass Transfer, 1998, 41(22): 3469-3482.
[12] Whitehouse D J. Surfaces and their Measurement[M]. CRC Press, 2002.
[13] Dong W P, Mainsah E, Stoutt K J. Determination of appropriate sampling conditions for three-dimensional microtopography measurement[J]. International Journal of Machine Tools and Manufacture, 1996, 36(12): 1347-1362.
[14] Liu S, Wang C, Yong R. Determining the optimal sampling interval for 3D morphology measurements of different-sized natural rock joints[J]. Measurement, 2024, 230: 114522.
[15] Jawaid A, Seewig J. Model of rough surfaces with Gaussian processes[J]. Surface Topography: Metrology and Properties, 2023, 11(1): 015013.
[16] Ghanem R G, Spanos P D. Spectral stochastic finite-element formulation for reliability analysis[J]. Journal of Engineering Mechanics, 1991, 117(10): 2351-2372.
[17] Thomas M U. A generalized maximum entropy principle[J]. Operations Research, 1979, 27(6): 1188-1196.
[18] Neal R M, Rosenthal J S. Efficiency of reversible MCMC methods: elementary derivations and applications to composite methods[J]. Journal of Applied Probability, 2025, 62(1): 188-208.
[19] Han F, Wei H, Liu Y. Thermal–mechanical coupling analysis of wheel–rail sliding friction under two-point contact conditions[J]. Lubricants, 2023, 11(5): 232.
[20] Jiang Y, Zhao P, Wu W. Thermoelastic contact of layer-substrate system: Effects of force-like interface and Kapitza thermal resistance models[J]. Composite Structures, 2025, 352: 118675.
[21] Ubero-Martínez I, Rodríguez-Tembleque L, Cifuentes-Rodríguez J, et al. 3D thermoelastic solids under non-linear interface thermal and orthotropic frictional contact conditions[J]. International Journal for Numerical Methods in Engineering, 2022, 123(11): 2631-2659.
[22] Rabinowicz E. The nature of the static and kinetic coefficients of friction[J]. Journal of applied physics, 1951, 22(11): 1373-1379.
[23] Khan K A, Tariq A. Thermal contact conductance and thermal rectification at elevated temperature using infrared thermography[J]. International Journal of Thermal Sciences, 2026, 221: 110440.